Comparison between x-ray scattering and velocity-interferometry measurements from shocked liquid deuterium

K. Falk,[1,2] S. P. Regan,[3] J. Vorberger,[4] B. J. B. Crowley,[1,5] S. H. Glenzer,[6] S. X. Hu,[3] C. D. Murphy,[1,7] P. B. Radha,[3] A. P. Jephcoat,[8,9] J. S. Wark,[1] D. O. Gericke,[4] and G. Gregori[1]

[1]*Department of Physics, Clarendon Laboratory, University of Oxford, Oxford, OX1 3PU, United Kingdom*

[2]*Los Alamos National Laboratory, Los Alamos, New Mexico 87545, USA*

[3]*Laboratory for Laser Energetics, University of Rochester, 250 E River Road, Rochester, New York 14623, USA*

[4]*Centre for Fusion, Space and Astrophysics, Department of Physics, Warwick University, Coventry CV4 7AL, United Kingdom*

[5]*AWE PLC, Aldermarston, Reading, RG7 4PR, United Kingdom*

[6]*Lawrence Livermore National Laboratory, P.O. Box 808, Livermore, California 94551, USA*

[7]*SUPA, School of Physics and Astronomy, University of Edinburgh, Edinburgh, EH9 3JZ, United Kingdom*

[8]*Diamond Light Source, Harwell Science and Innovation Campus, Chilton, OX11 0DE, United Kingdom*

[9]*Department of Earth Sciences, University of Oxford, Oxford, OX1 3PR, United Kingdom*

(Received 19 November 2012; revised manuscript received 2 February 2013; published 25 April 2013)

The equation of state of light elements is essential to understand the structure of Jovian planets and inertial confinement fusion research. The Omega laser was used to drive a planar shock wave in the cryogenically cooled deuterium, creating warm dense matter conditions. X-ray scattering was used to determine the spectrum near the boundary of the collective and noncollective scattering regimes using a narrow band x-ray source in backscattering geometry. Our scattering spectra are thus sensitive to the individual electron motion as well as the collective plasma behavior and provide a measurement of the electron density, temperature, and ionization state. Our data are consistent with velocity-interferometry measurements previously taken on the same shocked deuterium conditions and presented by K. Falk *et al*. [High Energy Density Phys. **8**, 76 (2012)]. This work presents a comparison of the two diagnostic systems and offers a detailed discussion of challenges encountered.

DOI: 10.1103/PhysRevE.87.043112 PACS number(s): 52.27.Gr, 62.50.−p, 64.30.−t, 61.20.−p

I. INTRODUCTION

Understanding of the microscopic structure of strongly interacting systems such as warm dense matter (WDM) remains one of the grand challenges of contemporary physics. In particular, the properties of light elements such as the hydrogen isotopes, helium, or carbon under extreme conditions with pressures reaching the Mbar regime and temperatures of the order of 0.1 to 10 eV are of great interest to current fundamental physics. In these systems, quantum degeneracy and strong interparticle forces determine the equation of state (EOS). This in turn governs the thermodynamics and macroscopic structure of many astrophysical objects including the giant gaseous planets and brown dwarfs [1–5] as well as the implosion of deuterium-tritium-fuel pellets in inertial confinement fusion (ICF) [6–9].

The theoretical description of the EOS of WDM is extremely challenging as these models must tackle a number of important questions such as the existence of the plasma phase transition, metallization, molecular-to-atomic transition, and melting of hydrogen at very high pressures and require many approximations or computational power not yet available [3]. All these complications result in disagreements between various approaches and individual models. Experimental validation of predictions made by theory is therefore essential.

High energy laser and pulsed power facilities have emerged as a tool to heat and compress liquid and solid targets to create conditions relevant to planetary interiors by driving fast shocks within the target composited of the studied material [10–13]. Velocity interferometry (VISAR) [14,15] in conjunction with streaked optical pyrometry (SOP) [16,17] have proven to be powerful techniques capable of providing a reliable measurement of the thermodynamic conditions in the shock [19]. VISAR employs a laser to directly measure the shock velocity from the Doppler shift of the light reflected by the critical surface on the moving shock front. SOP provides a complementary temperature measurement from the self-emission of the compressed material.

More recently, the new technique of x-ray Thomson scattering has rapidly expanded within high energy density physics as high energy photons are capable of penetrating deep inside WDM states reaching solid densities and higher, far beyond the density regions through which the conventional optical probes can propagate [18,20–23]. Here, a full set of thermodynamic conditions including the temperature and density measurement as well as information on the microscopic properties such as the ionization, interparticle collisions, and quantum effects can be extracted from a scattering spectrum [10,24,25].

This work presents a comparison between x-ray Thomson scattering (XRTS) measurements and independent VISAR and SOP diagnostics on the same experimental platform. While the VISAR results have already been discussed in Ref. [19], this paper focuses on the interpretation of the scattering data, as well as the required modeling framework based on density-functional molecular dynamics (DFT-MD) simulations [26–30].

In Sec. II, we will introduce the basic concepts of x-ray scattering and theoretical background of strongly coupled plasmas. Section III outlines the experimental setup. In Sec. IV, we shall discuss the results of the x-ray scattering from deuterium. Discussion of the XRTS results and comparison with VISAR is provided in Sec. V. This paper is then concluded in Sec. VI, where its implications for cryogenic D_2 measurements are presented.

II. THEORY

A. Basic definitions

The ion subsystem within the WDM state can be characterized in the temperature-density space through the ion-ion coupling parameter Γ_{ii}, which is the ratio of the average potential energy to the average thermal energy [31]. The classical coupling parameter is given by

$$\Gamma_{ii} = \frac{Z^2 e^2}{d_i k_B T}, \tag{1}$$

where Z is the charge of the ion and $d_i = [3/(4\pi n_i)]^{1/3}$ is the interion distance with the ion density n_i; here e is the elementary charge. The Coulomb interaction in the system is dominating for $\Gamma_{ii} \geqslant 1$ and the plasma is then considered strongly coupled. For typical dense plasma conditions applicable to planetary interiors, the ions are strongly coupled and always nondegenerate since their thermal de Broglie wavelength is much smaller than the average interparticle distance [32].

The electrons, on the other hand, are quantum particles following Fermi statistics. When the thermal energy of the electrons becomes comparable to the Fermi energy $E_F = (\hbar^2/2m_e)(3\pi^2 n_e)^{2/3}$, where n_e is the number density of the electrons and m_e is the electron mass, degeneracy effects have to be taken into account [10]. The degree of degeneracy is estimated by the ratio of thermal to Fermi energy

$$\Theta = \frac{k_B T_e}{E_F}. \tag{2}$$

In a degenerate plasma, Θ is smaller than unity.

Whereas in a nondegenerate electron gas the electron coupling can be estimated using the coupling parameter Γ_{ee} as in Eq. (1), in a degenerate quantum electron gas, the electron coupling is measured by the Wigner-Seitz parameter $r_s = d_e/a_B$ with the electron separation $d_e = [3/(4\pi n_e)]^{1/3}$. Here, a_B is the Bohr radius.

The electrons in WDM created in laser shock experiments with solid or liquid targets are fully or partially degenerate. Typical values achieved in experiments described in this work are $\Theta = 0.1$–2.5, $r_s = 2$–3, and $\Gamma = 0.6$–10.

To account for partial degeneracy of the electron gas, the inverse of the screening length $\kappa_e = 1/\lambda_s$ should be calculated from $\kappa_e^2 = (4e^2 m_e)/(\pi\hbar^3)\int f_e(p)\,dp$, where $f_e(p)$ is the Fermi distribution [33]. This formula includes the nondegenerate limit in which $\lambda_s = \sqrt{k_B T_e/4\pi e^2 n_e}$, as well as the case of high degeneracy in which the screening is given by the Thomas-Fermi screening length $\lambda_{\mathrm{TF}} = \sqrt{E_F/6\pi n_e e^2}$ [34–36]. A useful approximation is given by the use of a Debye form with an effective temperature [37,38]

$$\lambda_s = \sqrt{\frac{k_B T_e^{\mathrm{eff}}}{4\pi e^2 n_e}} \tag{3}$$

with $T_e^{\mathrm{eff}} = [T_e^4 + (\frac{2}{3}T_F)^4]^{1/4}$, which interpolates between the Debye and Thomas-Fermi screening length and yields results with less than 2% error for all densities [33].

The scattering wave number k in the nonrelativistic limit ($\hbar\omega \ll \hbar\omega_0$) is defined as the difference between the wave numbers of the incident and scattered electromagnetic waves

$$k = k_0 - k_1 = \frac{4\pi}{\lambda_0}\sin(\theta/2) \tag{4}$$

with θ being the scattering angle, λ_0 is the probe wavelength, k_0 and k_1 are the wave numbers of the incident and scattered x rays. Here, the frequency of incident and scattered photon is ω_0 and ω_1, respectively. For very high energy x rays, a photon transfers average momentum $\hbar\mathbf{k}$ and energy $\hbar\omega = \hbar\omega_0 - \hbar\omega_1 = E_C = \hbar^2 k^2/2m_e$ to a free electron upon their interaction, which corresponds to the Compton recoil. Strongly bound electrons scatter x rays elastically [10,32].

Photons can scatter from either individual electrons or from the collective electronic motion (plasmons) depending on the scale length over which the scattering is performed [10]. Therefore, the scattering parameter $\alpha = 1/k\lambda_s$ is introduced to establish the limit between the collective and noncollective scattering, where λ_s denotes the distance over which charges are screened in the plasma. For $\alpha < 1$, the scattering length $\lambda = 2\pi/k$ is smaller than the screening length λ_s and the x-rays scatter of the individual electrons. The measured spectrum then reflects the noncollective properties of the material [20]. If $\alpha > 1$, the probe scatters from the collective motion of the plasma, i.e., the plasmon oscillations close to the plasma frequency $\omega_p = \sqrt{4\pi n_e e^2/m_e}$, which gives the downshifted feature a characteristic n_e dependence [21].

B. Features in scattering spectrum

The scattering cross section can be described in terms of the dynamic structure factor $S(k,\omega)$, which is the Fourier transform of the intermediate scattering function

$$\frac{d^2\sigma}{d\Omega\, d\omega} = \sigma_T \frac{k_1}{k_0} S(k,\omega), \tag{5}$$

where σ_T is the Thomson cross section [39]. The measured scattered power therefore is directly proportional to $S(k,\omega)$ and the measured scattering spectrum contains information about the microscopic structure of the studied material [10,31,32]. The spectrum is made of independent contributions from bound and free electrons as described in a redmodel by Chihara [39]. In the case of nearly fully ionized deuterium, or when the Compton energy is larger than the binding energy of the bound electrons, the dynamic structure factor is given by

$$S(k,\omega) = |f_I(k) + q(k)|^2 S_{ii}(k,\omega) + Z S_{ee}^0(k,\omega). \tag{6}$$

The first term describes correlations of electrons that dynamically follow the ionic motion, i.e., bound or valence electrons, with $f_I(k)$ being the ion form factor, $q(k)$ describing the electronic screening of the ions, and $S_{ii}(k,\omega)$ is the ion-ion structure factor, which reflects the motion of the ions [10]. The term gives rise to the elastic Rayleigh peak and is usually taken to be static ($\omega = 0$) due to lack of frequency resolution on the scales of the ion plasma frequency. The second term describes the contribution of the free electrons, where Z is the number of delocalized electrons per nucleus and $S_{ee}^0(k,\omega)$ the Fourier transform of the electron-electron correlation function [10,31]. These electrons undergoing free motion then produce inelastic

scattering of the x rays with a characteristic downshifted Compton peak and may show collective excitations.

The theoretical calculation of the static ion structure factor $S_{ii}(k)$ for dense plasmas is still very challenging. Classical techniques such as molecular dynamics or hypernetted chain (HNC) schemes require introduction of complicated effective electron-ion or ion-ion potentials [40,41]. Density-functional molecular dynamics (DFT-MD) calculations are in principle able to account for all the important physics, but are challenging numerically [42]. The electron-electron structure factor can be derived from the fluctuation-dissipation theorem [43]

$$S^0_{ee}(k,\omega) = \frac{\hbar}{\exp(-\hbar\omega/k_B T_e) - 1} \frac{k^2}{4\pi^2 e^2 n_e} \mathrm{Im}\left[\frac{1}{\varepsilon(k,\omega)}\right], \tag{7}$$

where $\varepsilon(k,\omega)$ is the electron dielectric function. For weakly coupled electrons ($\Gamma_{ee} < 1$ or $r_s < 1$), $\varepsilon(k,\omega)$ may be calculated using the random phase approximation (RPA) [44,45]. Even at higher electron coupling, RPA is still reasonable. Further, improved electron response functions based on the Mermin or local field correction approaches have been used with great success [25,31,46].

Based on previous VISAR and SOP measurements and modeling, we infer the scattering parameter $\alpha \sim 0.7$–1. Thus, in this backscattering geometry, spectrally resolved x-ray Thomson scattering accesses the boundary of collective and noncollective regimes making our measurement sensitive to the individual electron motion with some sensitivity to the collective plasma behavior. The form of the dynamic structure factor is largely given by the electron velocity distribution function, which in turn depends on the thermodynamic quantities of the medium [47]. Due to the relationship between the electron-electron structure factor and the dielectric function, the shape of the free electron Compton feature in the scattered probe radiation carries information of the electron density and temperature.

III. EXPERIMENT

The 60-beam, 30-kJ Omega laser system was used to create the WDM conditions by launching a single shock inside the planar liquid deuterium target driven by the rapidly expanding material as it is ablated from the laser-target interface [13]. The deuterium was kept inside a copper cryogenic cell with 8-μm-thick polyimide windows on either side at pressure $P_0 \sim 1.38 \times 10^5$ Pa and cooled down to 18 K forming a liquid inside the target increasing its initial density to $\rho_0 = 0.175$ g/cm^3. Figure 1 shows the target and laser setup for the scattering experiment presented in this paper [48]. The target was equipped with gold shields designed to block any direct x-ray emission from any other part of the target than the scattering channel.

The drive beams were frequency tripled providing the 3ω ($\lambda = 351$ nm) laser output to increase the laser-plasma coupling efficiency [49]. The UV laser drive consisted of six pairs of 1-ns laser pulses evenly divided into two cones around the target normal at angles of 23.2° and 47.8°. A flat intensity profile was created by phase plates and polarization smoothing [50]. These square pulses were then staggered in time forming

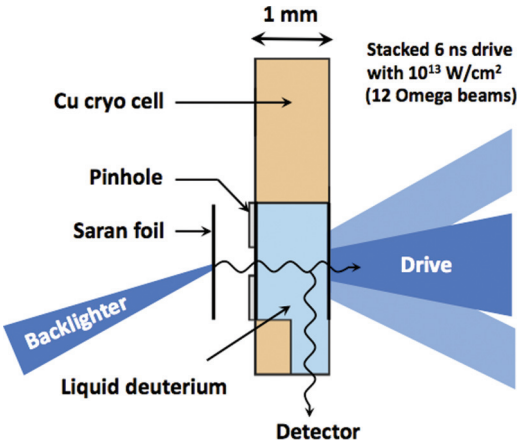

FIG. 1. (Color online) Schematic of the target setup with the laser drive and backlighter and scattering configuration. A constant intensity 6-ns laser drive incident on the CH ablator compresses and heats the material inside a planar layer of liquid deuterium target creating WDM. 16 tightly focused beams irradiate a saran backlighter with total intensity of 10^{16} W/cm^2. The scattered Cl Ly-α emission scattered at 90° down a 500-μm-wide scattering channel before it is detected with the XRFC outfitted with a HOPG crystal spectrometer [48].

6-ns constant drive with intensity of $\sim 10^{13}$ W/cm^2. The Omega system operates at 400–500 J/beam. The lower intensity drive used in this experiment (42 J/beam) is created by detuning of the frequency conversion crystals (FCC) lowering the conversion efficiency of the UV output of the laser.

Sixteen tightly focused 1-ns beams with a collective irradiance of 10^{16} W/cm^2 (200-μm focal spot) then come from the opposite side and irradiate a 12-μm-thick saran foil creating a burst of narrow-band Cl Ly-α x rays at 2.96 keV, which are used as our x-ray backlighter probe. The Ly-α radiation is emitted by highly ionized hydrogenlike atoms in the ablation plasma heated by inverse bremsstrahlung [10]. The backlighter lasers therefore operated at 3ω to maximize the conversion efficiency of the laser into x rays by reducing laser backscattering instabilities [49]. Since the conversion efficiency of desired Ly-α line relative to the He-like and Li-like satellites is improved as the laser intensity increases, no phase plates were installed in these beams to keep the focus of these beams as tight as possible [51]. These x rays are collimated by a 200-μm Ta pinhole and scattered at 90° to a gated Thomson spectrometer (GTS). The measurements of the Cl Ly-α line and its satellites are shown in Fig. 2. The direct spectral measurement of the probe line reveals a full-width at half-maximum (FWHM) of $\sim$9 eV with a Gaussian-type spectral profile.

The GTS is composed of a highly oriented pyrolytic graphite (HOPG) mosaic crystal (ZYB, 25 × 50 mm, 2 mm thick) [52] coupled to an x-ray framing camera (XRFC), which consists of a micro-channel-plate (MCP) combined with a CCD detector. The crystal was placed at the optimal Bragg angle of $\theta_B = 38.6°$ projecting the scattering spectra across the MCP camera which was placed 23.8 cm from the scattering target center, giving the spectrometer resolution of $\sim$12 eV/mm. The MCP has four individually powered strips charged in a sequence during the 1-ns backlighter

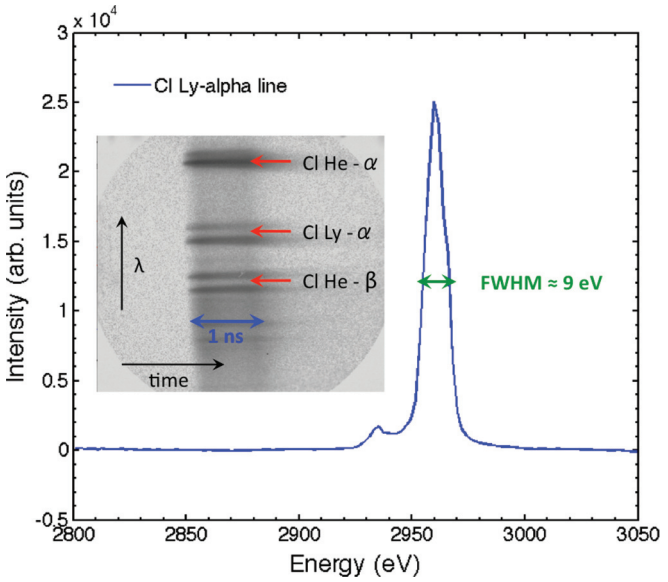

FIG. 2. (Color online) Cl Ly-α backlighter x-ray line at 2.96 keV as measured by the GTS spectrometer at Omega, the full-width at half-maximum (FWHM) spectral width of the line is ~9 eV. The inserted image shows a streaked spectrum of the emission lines created by the backlighter beams illuminating the saran foil.

flash. The integration time of each strip was 250 ps. Thanks to this capability, the temporal resolution of the scattering measurement was significantly improved and with it the signal-to-noise ratio [10]. A Be blast shield was used to block any visible radiation and stop any debris from damaging the spectrometer.

In addition to XRTS, velocity interferometry (VISAR) was used to measure the shock velocity in the deuterium sample. We used the same platform to the XRTS setup as shown in Fig. 3, with the only difference that the backlighted beams, saran foil, and pinhole were replaced by the interferometry laser (see Ref. [19] for a detailed discussion). The line-VISAR system at Omega operates at 532 nm. The system has two separate interferometer arms with different sensitivities (different

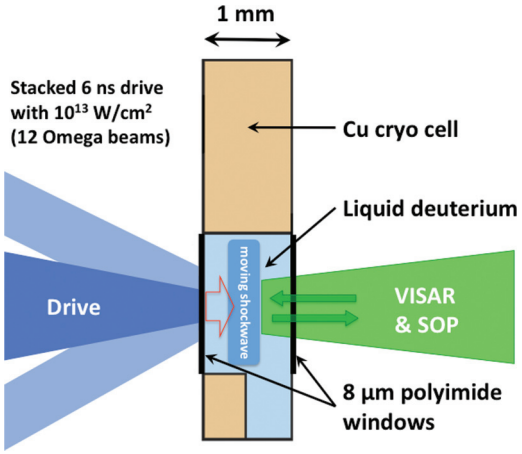

FIG. 3. (Color online) Schematic of the target setup with the laser drive and VISAR and SOP configurations. Due to fixed location of the VISAR telescope, the laser drive was switched to an opposite side of the Omega chamber, with the laser conditions unchanged.

optical delays), so that the velocity measurements from the independent interferometers can be matched to remove the 2π phase discontinuities in fast shock measurements [15]. This system produces a continuous record of the shock velocity history as well as a one-dimensional (1D) image of the spatial profile of the shock. The final shock diameter was measured by VISAR and was found to be 830 ± 30 μm which is consistent with best-focus spot size expected for Omega beams when phase plates have been used (600–800 μm) [19]. In addition, streaked optical pyrometry (SOP) diagnostic recorded self-emission from the shock front in a narrow wavelength band (590–850 nm) around $\lambda_0 = 684$ nm [16,17]. The SOP data were used to measure the temperature of the shocked material by comparing the measured emission intensity with a black or gray body radiation distribution [19]. The VISAR and SOP measurements provided shock velocity of 16.9 ± 0.9 km/s (corresponding to shock pressure of 37.5 GPa and mass density $\rho_s = 0.72$ g/cm^3) and radiation temperature $T_{SOP} = 0.57 \pm 0.05$ eV [19].

IV. RESULTS

A. Equation of state model

The deuterium equation of state used in this work was computed using first-principles density-functional molecular dynamics (DFT-MD) simulations within the *physical picture* with electrons and ions handled as elementary particles [26,27]. In this approach, the nuclei are treated by classical molecular dynamics simulations. Properties of the electrons are calculated via density-functional theory using a Mermin functional that accounts for temperature effects within the electron subsystem in a statistical sense. The dynamics of ions and electrons is effectively decoupled with the Born-Oppenheimer approximation. This description of hydrogen avoids most approximations concerning the composition and mixing necessary in *chemical models* [26].

For our DFT-MD simulations, we use the VASP package [53] (simulation parameters are similar to Ref. [26]). The main difference is that we here used a Mermin functional to account for the finite electron temperature. VASP also allows for the application of the projector augmented wave (PAW) potential [54]. This approach was verified by independent VISAR and SOP data in a previous experiment confirming that DFT-MD EOS was the only one of among the compared models providing a self-consistent treatment of the experimental data [19]. DFT-MD simulations have also proven to be a correct approach to model WDM with significant degeneracy and ion coupling effects in other experiments [23,55].

Due to their fundamental approach, the DFT-MD simulations provide an equation of state model, which is particularly strong in the degenerate strongly coupled plasma regime, which other EOS models treat by interpolation [56,57]. For this reason, these simulations have been chosen as an adequate EOS to describe the deuterium in the experiments presented in this work. The DFT-MD EOS can be combined with the experimental measurements including XRTS, VISAR, and SOP in order to provide a full set of thermodynamic conditions as well as provide an insight into the microscopic structure of WDM deuterium.

B. XRTS, VISAR, and SOP measurements

A number of scattering spectra from different shots were compared [19,22]. In order to avoid blanking of VISAR, the intensity of the drive laser had to be kept low at $\sim 10^{13}$ W/cm^2, minimizing the shock speed and with it the preheat of the material before the shock front. Thus, the shock wave did not propagate through the entire width of the scattering channel, leaving a large amount of cold material within the field of view of the spectrometer. In order to minimize the contribution of scattering from the cold material, the XRTS measurement was carried out at the end of the laser drive at 6 ns. Even then, simulations show that a large amount of cold material can contribute to the scattering measurement. As a result of this signal contamination, a sophisticated analysis which includes bound-free contribution from the unshocked material is needed. This requires an additional term in Eq. (6) to correctly calculate the contribution from bound-free transitions to the scattering spectra [10,32].

As no pusher was used, it is reasonable to assume that the conditions on the shock front are somewhat different from those behind it. With the aid of hydrodynamic simulations, we extracted the following conditions in the bulk of dense shock from XRTS measurement carried out at 6 ns: electron density in the range of 1.0–2.0 $\times$ 10^{23} cm^{-3}, temperature of $\sim$1–5 eV, and ionization $Z = 0.6$–0.9. The spread of the quoted values is constrained by the hydrosimulations. The method of obtaining these values is described in more detail in the following section.

The pressure and density measurement was extracted from the VISAR shock velocity measurement by applying the Hugoniot single-shock equation for known initial conditions by direct comparison with EOS tables [19,58]. This analysis is based on three different theoretical EOS models: (i) the SESAME tables [56], widely used for ICF applications; (ii) the model by Saumon and Chabrier (SC) that spans a wide range of conditions and is often used for astrophysical purposes [57]; and (iii) density-functional molecular dynamics (DFT-MD) simulations of fluid hydrogen [26,27]. The results from the individual models and the full analysis are presented in detail in Ref. [19]. This method offers an alternative to impedance matching (IM) techniques, where the shocked conditions are extracted from a particle velocity match on a surface of a quartz or Al pusher [11]. Such a pusher can not be used in conjunction with XRTS as it would cause significant contamination of the scattering signal from deuterium.

The shock front temperature was then obtained by comparing the measured emission intensity from the calibrated SOP diagnostic with a gray body radiation distribution [16,17]. The reflectivity of the shock under the given conditions was calculated from the EOS models [19]. This measurement was compared to theoretical predictions for temperature from the EOS models used to analyze the VISAR data. Only the DFT-MD calculations are consistent with the SOP temperature measurement. It can therefore be concluded that only the *ab initio* DFT-MD model was able to satisfy the constraints set by the shock velocity and temperature measurements, i.e., the self-consistency is constrained by one model satisfying both independent measurements as shown in Ref. [19]. From the optical measurements of the shock surface, we obtained a density $\rho = 0.72 \pm 0.01$ g/cm^3 and pressure 37.5 ± 3.9 GPa by combining the VISAR velocity measurement with DFT-MD EOS, and temperature of 0.57 ± 0.05 eV directly measured by SOP [19]. From the DFT-MD simulations, we estimated the ionization to be 0.7–1 corresponding to an electron density of $2.15 \times 10^{23} \pm 20\%$ cm^{-3}, which is in excellent agreement with experimental data presented in Ref. [59]. These values are also in good agreement with HELIOS simulations which give an electron density of $\sim 1.0 \times 10^{23}$ cm^{-3}, temperature of $\sim$1 eV, and ionization in the range of 0.3–0.7. The HELIOS simulations are consistent with earlier two-dimensional (2D) DRACO [60] and 1D LILAC [61] simulations presented in Refs. [48] and [22].

The electron densities and temperatures measured in the different experiments, including both VISAR and SOP as well as x-ray scattering runs, ranged between 1.0 and 2.15 $\times$ 10^{23} cm^{-3} and $\sim$0.6–5 eV, a set of WDM conditions directly relevant to the interiors of giant gaseous planets [4,5]. It should be noted that the optical diagnostics (VISAR and SOP) measured different conditions than XRTS. While VISAR and SOP are only sensitive to the Hugoniot conditions on the shock front, XRTS measures conditions in the whole bulk of the target.

V. DISCUSSION

A. Comparison with hydrosimulations

A series of 1D radiation-magnetohydrodynamics simulations using the HELIOS code [62] were run to compare theoretical predictions for the thermodynamic conditions within the shocked region in the deuterium at both intensities with the scattering measurements. The planar target is divided into spatial zones with the layer structure, material, and density as starting conditions specified upon the input. The code evolves the plasma within the Lagrangian hydrodynamics coordinate system in which the spatial grid moves with the fluid, i.e., cells maintain their mass ratio throughout the simulation. Radiative transport was calculated using a multifrequency flux-limited diffusion model with 50 frequency groups [62]. The Spitzer thermal conductivity model was selected [63]. HELIOS supports the PROPACEOS (PRism OPACity and Equation Of State) EOS and multigroup opacity data tables as well as the SESAME EOS [56]. Both equation of state models are based on the same theoretical assumptions and provide a similar result.

The actual calorimetry measurement of the laser drive was used as an input into the HELIOS simulation (see Fig. 4). These simulations were cross checked with previous VISAR and SOP measurements to constrain the margin of the simulation [19]. The shock velocity in the simulation was 16–19 km/s matching well with the VISAR measurement of 16.9 km/s. The shock surface temperature was found to be $\sim$1 eV, which is in a reasonable agreement with the SOP measurement of 0.57 ± 0.05 eV. The simulations also predict a somewhat high ionization for these conditions of $Z = 0.5$ or higher, which is consistent with previous findings in Ref. [19]. For this laser drive, all simulations show that a relatively slow and narrow shock wave forms, leaving a large bulk of cold unshocked material in the scattering channel.

A single scattering profile calculated within the RPA can not be used here as the bulk of the molecular deuterium adds a

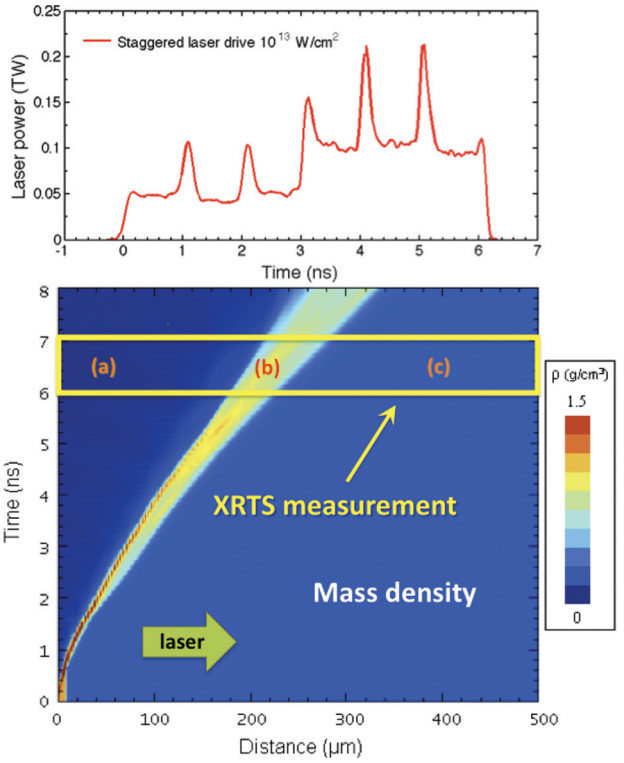

FIG. 4. (Color online) Result of 1D hydrosimulations using the HELIOS package for laser drive at 10^{13} W/cm^2. The laser input for the simulation was the calorimetry measurement from the experiment (upper plot). The scattering measurement is taken at ~6.5 ns from the start of the laser drive, marked by the rectangular box. The three regions within the field of view of the spectrometer correspond to the low density corona (a), dense shocked material (b), and a bulk of unshocked cold deuterium (c).

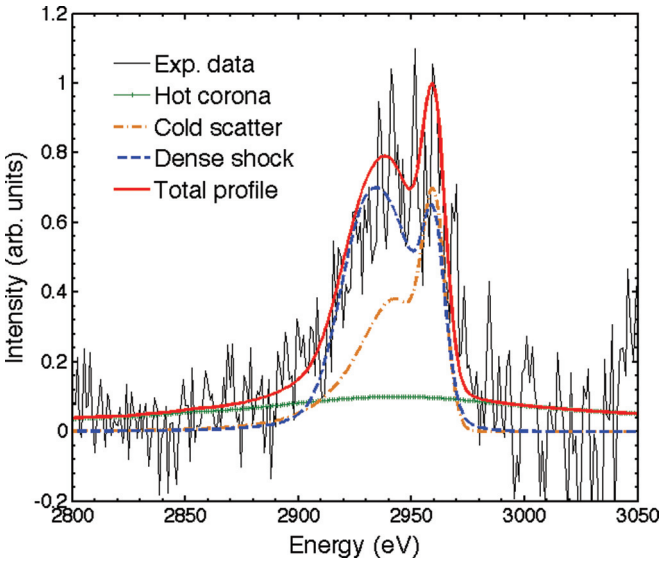

FIG. 5. (Color online) Experimental data overlayed with calculated plots for the hot expanding corona of low density [cross-dashed (green) line] with conditions of $\rho \sim 0.05$–0.005 g/cm^3, $T_e =$ 50–500 eV, $Z = 1$; cold deuterium [dotted-dashed (gold) line] where $\rho = 0.175$ g/cm^3, $T_e = 18$ K, $Z = 0$; and the dense shock [dashed (blue) line] with mass density $\rho \sim 0.7$–0.8 g/cm^3, $T_e = 0.7$–5 eV, $Z = 0.6$–1. Each contribution was weighted by its mass density and relative volume. The total composite profile [thick (red) line] was obtained by adding all of the weighted contributions and scaling it to overlap the experimental data.

contribution of the bound-free transitions to the total scattering spectrum. If one wishes to fit both the inelastic electron and elastic ion features to include these transitions in the scattering spectrum, a very low ionization state (around 10%) has to be assumed, which is not physical. However, previous results from SOP and DFT-MD simulations suggest very high ionization of around 70% for the conditions of the shock wave, which is consistent with reflectivity measurements by Celliers *et al.* [59] showing that around the shock velocity of 20 km/s the reflectivity of deuterium reaches its maximum, suggesting near full ionization in this region. This discrepancy is resolved at once if one looks at the individual contributions to the total scattering signal from different regions within the field of view of the spectrometer.

The output of the HELIOS simulation was used as an aid to extract the individual contributions from different spatial zones within the 500-μm side scattering channel. The simulations show that x rays can scatter over a very wide range of plasma conditions, which can be separated into three main regions contributing to the total scattering signal. These are the dense shocked material (mass density $\rho \sim 0.7$–0.8 g/cm^3, $T_e = 0.7 - 5$ eV, $Z = 0.6$–1), the hot expanding corona of low density behind the shock ($\rho \sim 0.05$–0.005 g/cm^3, $T_e =$ 50–500 eV, $Z = 1$), and the bulk of cold unshocked material before the shock wave ($\rho = 0.175$ g/cm^3, $T_e = 18$ K, $Z = 0$).

The output of the simulations was then used to calculate a synthetic scattering profile expected for each region. These profiles were then weighted by their mass density and relative volume to scale the relative contributions to the total signal:

$$S_{tot}(k,\omega) = \sum_j \rho_j w_j S_j(k,\omega), \tag{8}$$

where ρ_j, w_j, and $S_j(k,\omega)$ are the mass density, width, and scattering profile of zone j, respectively. These profiles were then added up and overlapped with the experimental scattering spectrum with an excellent agreement. All the contributions are shown in Fig. 5. This result confirms that the measured scattering spectrum can not be fitted with a single calculated profile due to the significant contribution of the cold scattering.

The conditions within the bulk of the shocked region as given by the HELIOS simulation were $\rho \sim 0.7$–0.8 g/cm^3, $n_e = 1.0$–2.0×10^{23} cm^{-3}, $T_e \sim 1$–5 eV, and $Z = 0.6$–0.9, with conditions on the shock front (i.e., a narrow region of plasma in the front of the shock wave, to which the VISAR and SOP measurements are also sensitive) being $\rho \approx 0.7$ g/cm^3, $n_e \sim 1.0 \times 10^{23}$ cm^{-3}, $T_e \sim 1$ eV, and $Z = 0.3$–0.7. This is in a good agreement with previous VISAR and SOP measurements and the DFT-MD simulations ($\rho = 0.72 \pm 0.01$ g/cm^3, $n_e = 2.15 \times 10^{23} \pm 20\%$ cm^{-3}, $T_e = 0.57 \pm 0.05$ eV, and $Z \sim 0.7$–1) [19]. Thus, once the cold contribution to the scattering signal is removed, the x-ray scattering measurement provides a self-consistent EOS measurement with independent diagnostics supported both by hydrosimulations and DFT-MD simulations.

B. Plasma conditions

The conditions inferred from the scattering measurements yielded a range of values for the degeneracy parameter of $\Theta \sim 0.05$–0.6, Wigner-Seitz parameter $r_s \sim 2$–3, and an ionic coupling parameter $\Gamma_{ii} \sim 1.0$–20. The analysis confirms that the state of matter created falls into the WDM regime of moderately to strongly coupled, partially or fully degenerate plasma at conditions equivalent to the interiors of giant planets. Although the scattering spectra in this work are unable to distinguish between the individual EOS models in this regime, due to high noise levels and signal contamination, previous experiments and simulations suggest that the DFT-MD simulations provide an accurate description of such states [19,23] in contrast of models such as SESAME table [56] or the Saumon and Chabrier EOS model [57].

It should be stressed that the conditions measured by x-ray scattering are not strictly the Hugoniot conditions as measured by VISAR and SOP. An Al or quartz pusher is generally used during shock velocity measurement experiments, which maintains a steady shock wave with homogeneous conditions and minimizes the effects of preheat resulting from strong laser drives. However, such a pusher can not be used during scattering experiments as the stray scattering from the pusher itself would be significantly stronger than the signal from the deuterium and would render this measurement impossible. Therefore, no pusher was used in this experiment. The only reliable velocity measurements can be taken at the start of the drive when the effects of preheat from the laser are not significant and this measurement can still lie on the principal Hugoniot. A significant preheat from hard x rays and energetic particles generated at the laser-plasma interface would change the conditions downstream, complicating the velocity measurement and at extreme levels even results in blanking of the VISAR diagnostic. The scattering measurement is then taken at a much later time when the shock wave traveled the maximum distance within the scattering channel, so that the principal Hugoniot conditions are no longer satisfied. The scattering measurement is thus consistent with previous measurements by VISAR and SOP, but not identical. The previous VISAR and SOP measurements agreed with the DFT-MD equations of state, but XRTS is unable to resolve the difference between the EOS models in this experiment.

The total measured scattering signal consists of contributions from all areas of the scattering channel including any remaining cold material, the dense shock itself, and the coronal plasma behind the shock. The intensity of the scattering signal depends on the total number of scatterers and is thus proportional to the electron density and the total volume of the sample. The hot coronal plasma therefore contributes very little due to its low density and only offsets the total signal intensity by a small amount (as a result of the extreme broadening of the signal due to the high temperatures). The scattering from the dense shock depends mainly on the width of the shock and the maximum density achieved. The proportion of the scattering impurity from the cold material is then given by the position of the shock with respect to the edge of the scattering channel at the time of the measurement. If the total volume of the cold material is large enough, it can create a significant contribution even at lower density. Since the shock wave created during the lower intensity drive only traveled at $\sim$20 km/s and by the time the XRTS measurement was carried out, it only reached just over 100 μm into the 500 μm wide scattering channel, much of the cold material remains within the field of view of the spectrometer and the measured scattering signal contains a significant contribution from impurity scattering of unionized matter. Under such conditions, the XRTS analysis was aided by hydrosimulations. An instrument capable of imaging XRTS measurement with a good spatial resolution would greatly benefit this experiment as it could resolve scattering from different layers in the target [64]. Simultaneous collective and noncollective XRTS measurements, and the use of independent diagnostics to pin some of the measurables, e.g., mass density measurement from radiography, would also help to reduce the error bars on the scattering measurement.

In the case of the higher intensity drive at 10^{14} W/cm^2 as in Ref. [22], VISAR can not be used at all since without a pusher or filter material the preheat is too strong and VISAR blanks immediately. Thus, conditions in these experiments are never on the principal Hugoniot. The shock wave created in these experiments is, however, much faster and thicker, which means that it has traveled to the edge of the scattering channel by 4 ns from the start of the laser drive and the dense region from the majority of the probe x-rays scatter is much bigger, resulting in a stronger scattering signal originating from a single shocked region and all the other contributions from the corona and cold material are negligible. Such scattering signals could therefore be successfully fitted with a single calculated profile reliably retrieving the shocked conditions.

VI. CONCLUSIONS

This work presents a comparison of EOS measurements from x-ray Thomson scattering with VISAR and SOP data from warm dense deuterium. The measurement of the thermodynamic conditions confirms that moderately to strongly coupled plasma with a strong effect of degeneracy was created and the conditions are directly comparable with those found inside the interiors of Jovian planets. Self-consistent measurement with the independent diagnostics as well as the DFT-MD equation of state was made. However, due to large noise in the scattering data, more detailed comparison is impossible at the present time.

It has been discussed that the VISAR, SOP, and XRTS measurements are sensitive to conditions from different regions in the shocked deuterium. If a simultaneous measurement using all of the above diagnostics is desired, no higher Z pusher material can be used as it would add strong impurity to the scattering signal from deuterium, making the data analysis very difficult if not completely impossible if imaging XRTS is not available. Under such conditions, VISAR can only operate at lower shock velocities [19]. On the other hand, XRTS works better for stronger shocks in deuterium, where a thicker shock wave with a higher temperature is generated, minimizing any signal from cold material [22]. XRTS measurement at lower intensity drives is possible, however, the signal levels are lower and contamination from cold scattering is an issue. Careful target and laser drive design is thus crucial to the success of such an experiment.

The findings in this paper present a significant step towards a combined VISAR and x-ray scattering experiment which

can be applied to equation of state measurements relevant to laboratory astrophysics, the study of planetary interiors, as well inertial confinement fusion. The ultimate goal of our measurements is to be able to find a reliable and accurate diagnostic system capable of constraining EOS models, which are still suffering from many discrepancies. This work provides a starting platform towards achieving this goal.

ACKNOWLEDGMENTS

The work of K.F., C.D.M., J.S.W., and G.G. was supported by EPSRC (EP/G007187/1) and HiPER funds. J.V. and D.O.G. were supported by EPSRC Grant No. EP/D062837. Support by the US Department of Energy, Office of Inertial Confinement Fusion under cooperative Agreement No. DE-FC52-08NA28302, is also acknowledged.

[1] W. B. Hubbard, Science **214**, 145 (1981).
[2] T. Guillot, Science **286**, 72 (1999).
[3] T. Guillot, Annu. Rev. Earth Planet Sci. **33**, 493 (2005).
[4] B. Militzer *et al.*, Astrophys. J. Lett. **688**, L45 (2008).
[5] N. Nettelmann *et al.*, Astrophys. J. **683**, 1217 (2008).
[6] J. Nuckolls *et al.*, Nature (London) **239**, 139 (1972).
[7] J. Lindl, Phys. Plasmas **2**, 3933 (1995).
[8] R. L. McCrory *et al.*, Nucl. Fusion **45**, S283 (2005).
[9] S. X. Hu, B. Militzer, V. N. Goncharov, and S. Skupsky, Phys. Rev. Lett. **104**, 235003 (2010).
[10] S. H. Glenzer and R. Redmer, Rev. Mod. Phys. **81**, 1625 (2009).
[11] D. G. Hicks, T. R. Boehly, P. M. Celliers, J. H. Eggert, S. J. Moon, D. D. Meyerhofer, and G. W. Collins, Phys. Rev. B **79**, 014112 (2009).
[12] G. W. Collins *et al.*, Science **281**, 1178 (1998).
[13] T. R. Boehly *et al.*, Opt. Commun. **133**, 495 (1997).
[14] A. C. Forsman and G. A. Kyrala, Phys. Rev. E **63**, 056402 (2001).
[15] P. M. Celliers *et al.*, Rev. Sci. Instrum., **75**, 4916 (2004).
[16] J. E. Miller *et al.*, Rev. Sci. Instrum. **78**, 034903 (2007).
[17] J. E. Bailey, M. D. Knudson, A. L. Carlson, G. S. Dunham, M. P. Desjarlais, D. L. Hanson, and J. R. Asay, Phys. Rev. B **78**, 144107 (2008).
[18] S. H. Glenzer, G. Gregori, R. W. Lee, F. J. Rogers, S. W. Pollaine, and O. L. Landen, Phys. Rev. Lett. **90**, 175002 (2003).
[19] K. Falk *et al.*, High Energy Density Phys. **8**, 76 (2012).
[20] H. Sawada *et al.*, Phys. Plasmas **14**, 122703 (2007).
[21] S. H. Glenzer *et al.*, Phys. Rev. Lett. **98**, 065002 (2007).
[22] S. P. Regan *et al.*, Phys. Rev. Lett. **109**, 265003 (2012).
[23] E. García Saiz *et al.*, Nat. Phys. **4**, 940 (2008).
[24] B. Barbrel *et al.*, Phys. Rev. Lett. **102**, 165004 (2009).
[25] K. Falk *et al.*, J. Phys.: Conf. Ser. **244**, 042014 (2010).
[26] J. Vorberger, I. Tamblyn, B. Militzer, and S.A. Bonev, Phys. Rev. B **75**, 024206 (2007).
[27] J. Vorberger *et al.*, Contrib. Plasma Phys. **47**, 375 (2007).
[28] A. Grinenko, D. O. Gericke, S. H. Glenzer, and J. Vorberger, Phys. Rev. Lett. **101**, 194801 (2008).
[29] M. P. Desjarlais, Phys. Rev. B **68**, 064204 (2003).
[30] S. A. Bonev, B. Militzer, and G. Galli, Phys. Rev. B **69**, 014101 (2004).
[31] S. Ichimaru, Rev. Mod. Phys. **54**, 1017 (1982).
[32] G. Gregori, S. H. Glenzer, W. Rozmus, R. W. Lee, and O. L. Landen, Phys. Rev. E **67**, 026412 (2003).
[33] D. O. Gericke, J. Vorberger, K. Wünsch, and G. Gregori, Phys. Rev. E **81**, 065401(R) (2010).
[34] F. F. Chen, *Introduction to Plasma Physics and Controlled Fusion*, Vol. I, 2nd ed. (Plenum, New York, 1984).
[35] S. Galam and J. P. Hansen, Phys. Rev. A **14**, 2 (1976).
[36] R. L. Liboff, J. Appl. Phys. **56**, 9 (1984).
[37] M. W. C. Dharma-wardana and F. Perrot, Phys. Rev. Lett. **84**, 959 (2000).
[38] F. Perrot *et al.*, Phys. Rev. B **62**, 16536 (2000).
[39] J. Chihara, J. Phys. F: Met. Phys. **17**, 295 (1987); J. Phys.: Condens. Matter **12**, 231 (2000).
[40] K. Wünsch, P. Hilse, M. Schlanges, and D. O. Gericke, Phys. Rev. E **77**, 056404 (2008).
[41] V. Schwarz *et al.*, High Energy Density Phys. **6**, 305 (2010).
[42] K. Wünsch, J. Vorberger, and D. O. Gericke, Phys. Rev. E **79**, 010201(R) (2009).
[43] R. Kubo, J. Phys. Soc. Jpn. **12**, 570 (1957).
[44] D. Pines and D. Bohm, Phys. Rev. **85**, 338 (1952).
[45] D. Pines and P. Nozieres, *The Theory of Quantum Fluids* (Addison-Wesley, Redwood, CA, 1990).
[46] C. Fortmann, A. Wierling, and G. Ropke, Phys. Rev. E **81**, 026405 (2010).
[47] J. W. DuMond and H. A. Kirkpatrick, Phys. Rev. **37**, 136 (1931).
[48] S. P. Regan *et al.*, J. Phys.: Conf. Ser. **244**, 042017 (2010).
[49] W. L. Kruer, *The Physics of Laser Plasma Interactions* (Westview, Colorado, 2003).
[50] S. P. Regan *et al.*, J. Opt. Soc. Am. B **22**, 998 (2005).
[51] M. K. Urry *et al.*, J. Quant. Spectrosc. Radiat. Transf. **99**, 636 (2006).
[52] H. Legall *et al.*, J. Appl. Crystallogr. **42**, 572 (2009).
[53] G. Kresse and J. Furthmüller, Phys. Rev. B **54**, 11169 (1996).
[54] G. Kresse and D. Joubert, Phys. Rev. B **59**, 1758 (1999).
[55] A. Pelka *et al.*, Phys. Rev. Lett. **105**, 265701 (2010).
[56] G. I. Kerley, Phys. Earth Planet. Inter. **6**, 78 (1972).
[57] D. Saumon and G. Chabrier, Phys. Rev. Lett. **62**, 2397 (1989).
[58] Y. B. Zel'dovich and Y. P. Raizer, *Physics of Shock Waves and High Temperature Hydrodynamic Phenomena* (Dover, Mineola, NY, 2002).
[59] P. M. Celliers *et al.*, Phys. Rev. Lett. **84**, 5564 (2000).
[60] P. B. Radha *et al.*, Phys. Plasmas **12**, 056307 (2005).
[61] J. Delettrez *et al.*, Phys. Rev. A **36**, 3926 (1987).
[62] J. J. MacFarlane *et al.*, J. Quant. Spectrosc. Radiat. Transfer **99**, 381 (2006).
[63] L. Spitzer, Jr. and R. Härm, Phys. Rev. **89**, 977 (1953).
[64] E. J. Gamboa, D. S. Montgomery, I. M. Hall, and R. P. Drake, Journal of Instrumentation **6**, P04004 (2011); E. J. Gamboa *et al.*, Rev. Sci. Instrum. **83**, 10E108 (2012).